

Design of a Novel Hypersonic Inflatable Aerodynamic Decelerator for Mars Entry, Descent, and Landing

Nathaniel Skolnik, Hiromasa Kamezawa, Lin Li, Grant Rossman, Brandon Sforzo, Robert D. Braun
Georgia Institute of Technology

Entry, descent, and landing (EDL) is especially challenging on Mars because the atmosphere is too thin to provide substantial deceleration, but thick enough to generate significant heating during the reentry phase. As a result, innovative ideas are required to enable future high-mass Mars landing missions. One such promising approach is to use an inflatable aerodynamic decelerator (IAD). Compared with traditional rigid aeroshells, IADs are made of lightweight, flexible materials that can be folded into a smaller volume in the rocket payload fairing and inflated prior to atmospheric entry. Such IADs are able to reduce the ballistic coefficient and peak heating, providing an opportunity to land at higher surface elevations on Mars. Currently, NASA Langley Research Center is investigating the development of Hypersonic Inflatable Aerodynamic Decelerators (HIADs) to enable future large robotic and human exploration missions. Much of the previous work performed on HIADs has focused on symmetric shapes that fly through the atmosphere with ballistic trajectories or trajectories with low lift-to-drag ratios accomplished via CG-offset. The present investigation assesses the technical feasibility of a novel HIAD concept that can vary lift-to-drag ratios between 0.2 and 0.5, is aerodynamically stable between 0.6 km/s and 6.5 km/s, is extensible to aeroshell diameters of 15 to 20 meters, and possesses an approximately smooth outer mold line to avoid localized heating.

Nomenclature

A	= Amplitude of oscillation	dV	= Change in Volume
a	= Cylinder diameter	D	= Drag
α	= Angle of attack	D_0	= HIAD Major Diameter
β	= Bank angle	D_N	= Rigid Nose Diameter
C_p	= Pressure coefficient	δ	= Deflection
C_x	= Force coefficient in the x direction	F_A	= Aerodynamic Force
C_y	= Force coefficient in the y direction	θ	= Asymmetric Cone Angle
C_m	= Coefficient of Pitching Moment	θ_s	= Symmetric Cone Angle
C_l	= Coefficient of Rolling Moment	P	= Inflation Pressure
L	= Lift	ϕ	= Roll angle
L_V	= Vertical Component of Lift	σ	= Stress
L/D	= Lift to Drag Ratio	V_∞	= Free stream velocity

I. Introduction

Entry, descent, and landing (EDL) is especially challenging on Mars due the nature of the planet. The atmosphere on Mars is too thin (approximately 1% of Earth's density) to provide substantial deceleration, but thick enough to generate significant heating during the reentry phase. As a result, Mars entry vehicles have been constrained to land at lower surface elevations. Past successful Mars landers have relied on

Viking heritage technologies that are capable of delivering landed payloads of 0.9 (metric tons) at MOLA elevations below 0 (km).^{1,2} The most recent example was the Mars Science Laboratory (MSL) mission in 2012. Future human exploration missions will require much larger payload masses ranging from 20 (metric tons) to as much as 80 (metric tons) per landing event.¹ These missions will likely require the deployment of much larger drag devices in order to manage the ballistic coefficient. Such requirements cannot be achieved with Viking EDL technology since the maximum diameter of the rigid aeroshell is constrained by the diameter of the launch vehicle fairing.

As a result, innovative ideas are being studied in order to enable future Mars missions. One such promising approach is the use of an inflatable aerodynamic decelerator (IAD), originally developed in the 1960s.³⁻⁹ Compared with traditional rigid aeroshells, IADs are made of lightweight flexible materials that can be packaged into a smaller volume in the rocket fairing and inflated upon reentry. Such IADs are able to reduce the ballistic coefficient and peak heating, providing an opportunity to land at higher surface elevations on Mars. Currently, NASA Langley Research Center is investigating the development of Hypersonic Inflatable Aerodynamic Decelerators (HIADs) to enable future large robotic and human exploration missions. The majority of previous work on HIADs has focused on symmetric shapes that either fly along a ballistic trajectory, or at relatively low lift-to-drag ratios with a modest center-of-gravity (CG) offset. Many ground tests and flight-tests have been conducted to mature HIAD technology.¹⁰⁻¹⁶

It is known that lifting trajectories allow for shallower reentry, which reduce the peak heat rate and peak deceleration, as well as expand cross-range capabilities and improve landing accuracy. The most common method of generating lift for an axisymmetric entry vehicle is to use a CG-offset in order to fly at the desirable angle of attack. This approach was used, for example, by the Mars Science Laboratory mission. However, achieving an L/D ratio in this manner is costly from a mass and packaging perspective. Therefore, it is important to investigate alternative means of generating lift. One such alternative is to utilize an asymmetric entry body. This paper will present a method of choosing a mission specific asymmetric entry body, as well as supporting feasibility analysis on the chosen body shape. An investigation is also conducted into technology packages that would enable L/D to be modulated on demand during the flight.

II. Technical, Scientific Evaluation and Rationale of Proposed Concept

A. Aeroshell Configuration

Harper has performed analysis on the use of a shifted, asymmetric HIAD for future Mars missions, which allows higher L/D, in the range of 0.5, with angles of attack of -25° .¹⁷ This greatly increases vehicle landing mass capabilities and allows for a greater range of CG location that satisfy static stability about the pitch axis. In this investigation, a “100% shifted HIAD” design was chosen for analysis because of its ability to produce an L/D of 0.55 and angle of attack of -30° as found by Harper¹⁸ and to be able to have a smaller trim angle of attack. A smaller trim angle-of-attack is desirable because it requires less ballast mass, allows greater payload volume flexibility, and reduces aerothermal and lateral aerodynamic loading on the leeside of the HIAD.¹⁸ The appropriate HIAD shape was determined by conducting a thorough search of the geometry design space, which initially consisted of three variables at three levels. The design space was further narrowed to four cone angles once the major diameter and rigid diameter were found.

In addition to the 100% shifted HIAD design, a common cylindrical payload fairing (similar to the IRVE-3 centerbody) was extended directly backwards from the rigid heatshield just beyond the depth of the largest diameter tori. The benefits of adding this cylindrical payload fairing include its ability to support rigid attachments of the tori, provide a protected volume to insert the payload, support structural loads, and support the attachment and function of a viable Reaction Control System (RCS). A rigid core aeroshell caps one end of the cylindrical payload fairing, while the tori and fabric are attached where the rigid core aeroshell and the fairing meet.

B. Aerodynamic Analysis Method

A HIAD, primarily operating in a hypersonic regime, can be modeled using a Modified-Newtonian aerodynamic simulation to calculate aerodynamic forces within the velocity window of interest.²⁰ A Computational Fluid Dynamics (CFD) simulation was created for this investigation to estimate aerodynamic properties of the proposed HIAD concept. The following analysis approximates the ratio of specific heats (γ) in the Martian atmosphere to be 1.28 and independent of altitude.^{21, 22} The geometry selection process was performed for the hypersonic flow regime between Mach 5 and Mach 20 where $C_{P_{max}}$ was approximated as a constant.

C. HIAD Configuration

The HIAD geometry was determined by performing a thorough search of the geometry design space. Several design constraints were placed on the design space to ensure geometry feasibility, including the ability to generate an L/D of 0.5, the ability to achieve static pitch stability, and a CG location that resides within the cylindrical payload fairing. The L/D ratio of 0.5 is a mission specific value and can be varied based on the mission. The objective was to minimize the associated CG offset percentage from the centerline corresponding to each feasible design. In this study, the radius of the cylindrical payload fairing is considered to be a 100% shift from the centerline, which is the maximum feasible case. Additionally, there was an angle-of-attack constraint on the vehicle such that the stagnation point remained on the surface of the rigid heat shield. The coordinate system shown in Figure 1 was used throughout this paper. It is important to note that the x-axis passes through the centerline of the cylindrical payload fairing, the z-axis is tangent to the heatshield nose, and a positive angle of attack is defined as shown in Figure 1.

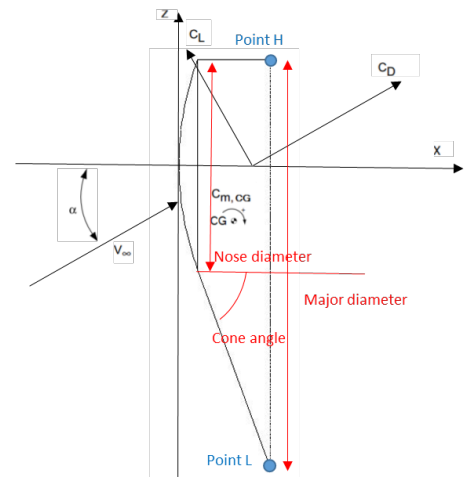


Figure 1: Aerodynamic Forces Exerted on the Vehicle in Body Coordinates

1. Relation between CG location and C_m

The optimization objective was to minimize the associated CG offset percentage from the centerline. Therefore, the relation between CG location and C_m should be mentioned before moving into the optimization itself since the C_m values are used to determine which geometry has the CG closest from the payload centerline. As the CG moves downward in the negative z-direction, the C_m increases shown in Figure 2. Thus it can be assumed that C_m closer zero has CG closer to centerline of the payload. The final optimized geometry were used here just to show that the assumption above can be validated.

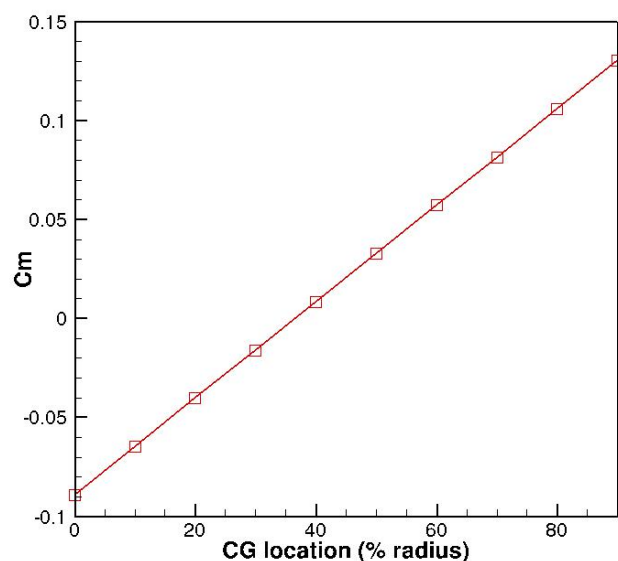


Figure 2. C_m versus HIAD CG location (% radius) with 60° cone angle, 15 m base diameter and 9 m nose diameter at -29° angle of attack.

2. Optimization with Taguchi Orthogonal Experimental Design

The cone angle (θ), diameter of the rigid nose cone (D_N), and the overall major diameter (D_0) are the three design variables used to define the geometry shown in Figure 1. Through use of a Taguchi L9 orthogonal array,²³ this optimization can be performed by assessing the 9 cases shown in Table 1. For each case, Modified Newtonian aerodynamic analysis was performed at Mach 20 and at 5° angle of attack increments from -30° to 10° .

Table 1: Configuration of HIAD Cases

Configuration	Cone Angle ($^\circ$)	Major Diameter (m)	Nose Diameter (m)
Case 1	50	15	7
Case 2	50	17.5	8
Case 3	50	20	9
Case 4	65	15	8
Case 5	65	17.5	9
Case 6	65	20	7
Case 7	80	15	9
Case 8	80	17.5	7
Case 9	80	20	8

The results of the Modified Newtonian aerodynamic analysis are shown in Figures 3 and 4, with all infeasible designs, based on the constraint for angle of attack previously mention, having been removed. Two trends were observed from the optimization process. First, the cone angle is the most influential variable on L/D as indicated by Figure 3. Second, a larger major diameter and smaller rigid nose diameter could generate geometry that can have C_m close to zero compared to others by Figure 4.

It can be found that the configuration that can have CG closer to centerline while satisfying L/D 0.5 from the design space have a cone angle of 65° .

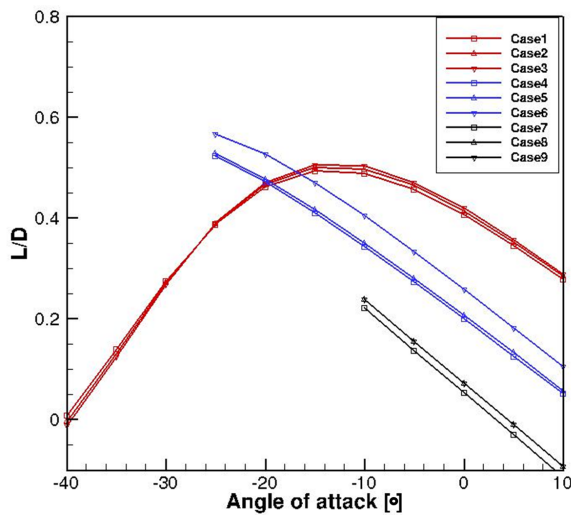


Figure 3: L/D versus Angle-of-Attack for Orthogonal Array.

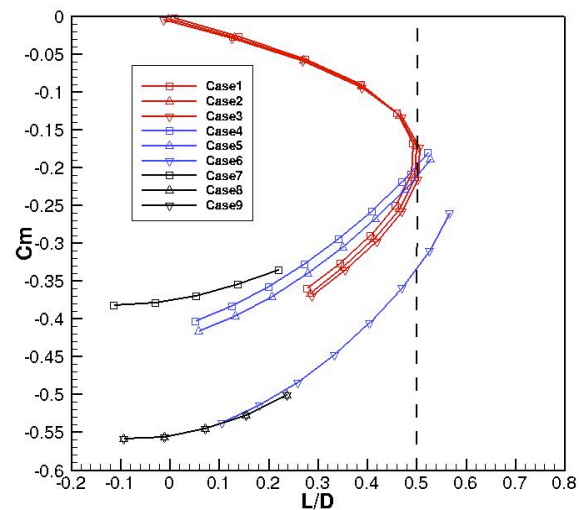


Figure 4: Coefficient of Moment versus L/D ratio for Orthogonal Array.

3. Refined Optimization on Nose and Base Diameter

From the first stage of analysis, it was determined that nose diameter and base diameter played an important role in the stability of the vehicle by reducing C_m . Therefore a second set of analyses was performed while holding the cone angle constant at 65° and varying the nose and base diameters. The configurations of the vehicles used in this analysis are seen in Table 2. After performing the Modified Newtonian aerodynamic analysis, as shown in Figure 5, two trends can be seen. Increasing the nose diameter reduces C_m for fixed base diameter and cone angle for all case. Reducing the base diameter reduces C_m for fixed nose diameter and cone angle for all cases. As the result, it was found that Case 3, with a nose diameter of 9 m and a base diameter of 15 m, had the smallest C_m in all cases of L/D and was thus thought to have CG closest to centerline of the payload.

Table 2: Configuration of HIAD Cases

Configuration	Cone Angle ($^\circ$)	Major Diameter (m)	Nose Diameter (m)
Case 1	65	15	7
Case 2	65	15	8
Case 3	65	15	9
Case 4	65	17.5	7
Case 5	65	17.5	8
Case 6	65	17.5	9
Case 7	65	20	7
Case 8	65	20	8
Case 9	65	20	9

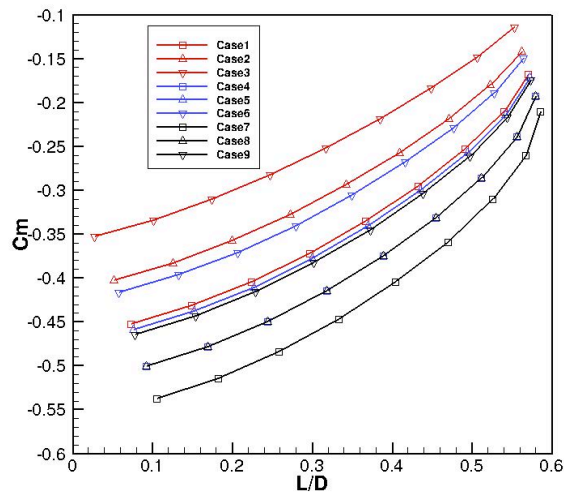


Figure 5: C_m versus L/D for Orthogonal Array for Nose and Base Diameter Down Selection.

4. Refined Optimization on Cone Angle

To further refine the geometry, a third down selection was performed using the base and nose diameters from Case 3 (15 m and 9 m, respectively) as the baseline, while parametrically varying the cone angle. Because the vehicle's cone angle most strongly influences L/D , it was varied between 50° and 65° , in 5° increments. A Modified-Newtonian aerodynamic analysis was performed on each shape in Table 3. Case 5-3 was selected as the best candidate because it produced the lowest C_m .

Table 3: Downselection of HIAD Cases and L/D Results

Configs.	Cone Angle ($^\circ$)	Major Diameter (m)	Nose Diameter (m)	C_m at $L/D = 0.5$	α_{trim} at $L/D = 0.5$
Case 3-1	50	15	9	---*	---*
Case 3-2	55	15	9	---*	---*
Case 3-3	60	15	9	-0.08	-29°
Case 3-4	65	15	9	-0.15	-24°

*geometries for Case3-1 and Case3-2 cannot achieve $L/D=0.5$ at any angle of attack

5. Pitch Static Stability Analysis

For the selected Case 3-3 configuration, the potential location of the center-of-gravity (CG) was determined and a resulting static stability analysis about the pitching axis was carried out. Static stability about the pitch axis is achieved when the following two requirements, shown in Equation 1 and Equation 2, are satisfied where C_m is the pitching moment coefficient and $C_{m_\alpha} = \frac{\partial C_m}{\partial \alpha}$:

$$C_m = 0.00 \quad (1)$$

$$C_{m_\alpha} < 0.00 \quad (2)$$

The result is shown in Figure 6. This is found to be static stable and have its CG 36% off from the centerline of the payload.

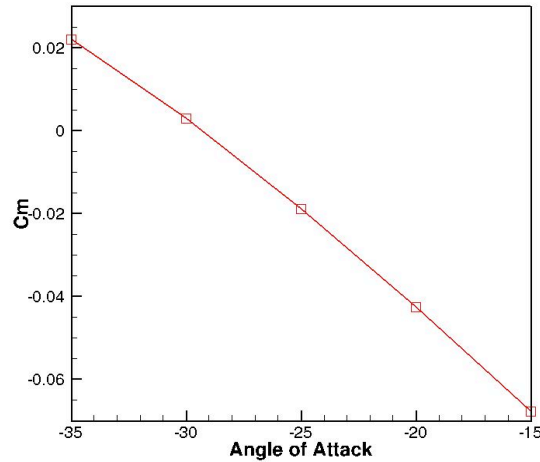


Figure 6. C_m versus Angle of Attack for Cone Angle of 60° Major Diameter of 15m and Rigid Diameter of 9 m HIAD with CG 36% off from the CG.

III. Feasibility of Proposed Concept of Idea, Design Simplicity, Required System Mass, and Extensibility to Large Scale Operation

A. Mass vs. Complexity Study

The asymmetric HIAD design chosen for detailed analysis has a 9 m diameter rigid nose cone (D_N), 65° cone angle (θ), and 15 (m) overall major diameter (D_0). The goal of the analysis presented in this section is to determine the total number of tori that would be employed in the final design based on two criteria: design simplicity and decelerator system mass. Design simplicity was assumed to be proportional to the number of components of the inflatable structure, which is equivalent to the total number of tori. For a given decelerator design, with a fixed mass of the rigid nose cone structure and thermal protection system, the decelerator system can be minimized by minimizing the mass of the inflatable structure. The two criteria were combined in an overall objective function by normalizing both quantities with respect to their maximum achieved max mass and max tori values and summing them with equal weight, as described in Equation 3. The goal was then to minimize this function.

$$f_{II}(\# \text{ of tori}) = \frac{\text{mass}(i) - \min(\text{mass})}{\max(\text{mass}) - \min(\text{mass})} + \frac{\text{tori} \# (i) - \min(\text{tori} \#)}{\max(\text{tori} \#) - \min(\text{tori} \#)} \quad (3)$$

The number of tori used in the final configuration was determined by the design that minimized the overall objective function. The sensitivity to different weightings of mass or simplicity on the objective function was also investigated to understand its effect on the final design parameters.

The inflatable structure mass consisted of two major components: the fabric and gas mass. It was assumed that Kevlar would be used to construct the tori and FlexShell cover, the same material that is used on the symmetric stacked tori configuration at NASA Langley Research Center.²⁴ Kevlar material properties are available from DuPont technical guides.²⁵ The tori inflation gas was assumed to be air with the inflation pressure of 15 psi determined based on the 6 (m) HIAD wind tunnel testing.²⁶ A summary of the parameters used in the inflatable structure mass calculation is shown in Table 4. Additionally, the maximum torus diameter was limited to 1 (m) and the minimum torus diameter was limited to 0.2 (m) to account for reasonable manufacturing capabilities. Designs were also limited to a maximum of 15 tori to constrain the design complexity.

Table 4: Material and Design Properties for Inflatable Structure

Gas Density (ρ_{gas}) ($\frac{kg}{m^3}$)	Inflation Pressure (psi)	Fabric Density (ρ_{fabric}) ($\frac{kg}{m^3}$)	Fabric Thickness (t) (mm)
1.2922 @ 1 atm	15	1150	1

The mass calculations were performed in Matlab, which allowed for an initial determination of the tori minor diameter. Because the tori lay tangent to each other along the shortest edge (L) of the decelerator, the minor diameter of the torus, $2r$, could be calculated by dividing the length, L , of the torus, by the number of tori, as seen in Figure 7. L is calculated based on θ , D_N , and D_0 , as described in Equation 4.

$$\text{Shortest Edge } (L) = \frac{(D_0 - D_N)}{\tan(\theta)} \quad (4)$$

Once r was calculated, the major diameter of the torus, $2R$, can be determined using Equation 5.

$$R(i) = \frac{1}{2} * (D_N + x_{\text{center}}(i) * \tan(\theta) + \frac{r}{\cos(\theta)} - r) \quad (5)$$

The total surface area, A_{total} , and volume, V_{total} , of the tori are determined using Equations 6 and 7, which then allow for the total mass, M_{total} , of the inflatable structure to be determined in Equation (8).

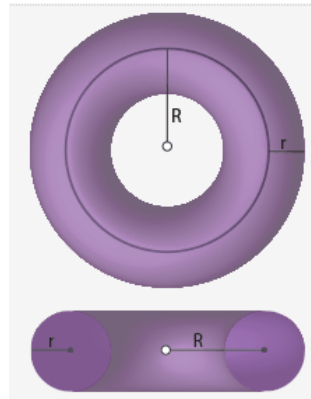
$$A_{\text{total}} = \sum_{i=1}^n (2 * \pi * R(i)) * (2 * \pi * r) \quad (6)$$

$$V_{\text{total}} = \sum_{i=1}^n (2 * \pi * R(i)) * (\pi * r^2) \quad (7)$$

$$M_{\text{total}} = D_g * V_{\text{total}} + D_f * A_{\text{total}} * t \quad (8)$$

In addition, the minimum required payload packing density, ρ_{packing} , can be calculated to evaluate the feasibility of the design, as shown in Equation 9. The calculations assumed that the payload has a cylindrical shape, is located behind the rigid nose cone, and that the length of the payload is the same as L .

$$\rho_{\text{packing}} = \frac{M_{\text{payload}}}{L * (\pi * (D_N - 2 * r)^2)} \quad (9)$$

**Figure 7: Geometry of a Torus²⁷**

The final design, as chosen based on the objective function in Equation 3, assumed that design simplicity was equally as important as the decelerator system mass. However, it is important to understand how that weighting affects the final design. A sensitivity analysis is required, and is done by adjusting the

weighting of each component in the objective function. Table 5 shows the final results of the objective function, leading to 8 tori being chosen for the design.

Table 5: Summary of Objective Function by Varying the Weighting Values

Total # of tori	4	5	6	7	8	9	10
r (m)	0.433	0.346	0.289	0.247	0.217	0.192	0.173
f_{II} (# of tori)	1.000	0.8468	0.7628	0.7231	0.713	0.7233	0.7485

B. Construction Method

Construction feasibility was also examined to ensure the proposed asymmetric shape could be built. A stacked tori method was chosen, as was utilized on the IRVE-3 test vehicle, to create the shifted shape. In the IRVE-3 test vehicle, the tori were stacked in a symmetric configuration, held in place with radial and pairing straps. The tori in the chosen design can be stacked similarly, but instead of a symmetric configuration only one point on the tori will be stacked. This configuration is demonstrated in the side view of Figure 8.

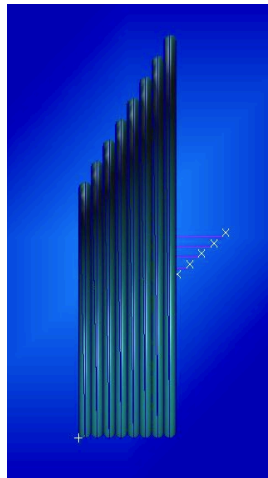


Figure 8: Side View of 100% Shifted HIAD

The shifted configuration shown poses a problem with how the tori would be held together. In the symmetric HIAD configuration the straps held the tori together as all attachment points were equally spaced from one another. In the shifted configuration, the tori get further from each other around the circumference. This means that straps would have to be differing lengths and shapes in order to lie flat along all tori. These straps would add design and construction complexity.

A proposed solution to this problem is a concept called the FlexShell, as shown in Figure 11. The FlexShell will be a continuous membrane of Kevlar that covers all of the HIAD tori. This layer will reside between the inflatable tori and the thermal protection system. The FlexShell will be cut such that it forms an outer shell to the desired shifted HIAD shape. This shell will then cover the inflated tori and they will have continuous attachment to the FlexShell, effectively distributing any aerodynamic forces as well as holding the tori into the desired shifted shape. The flex shell will also fill the gaps between tori created in the asymmetric design.

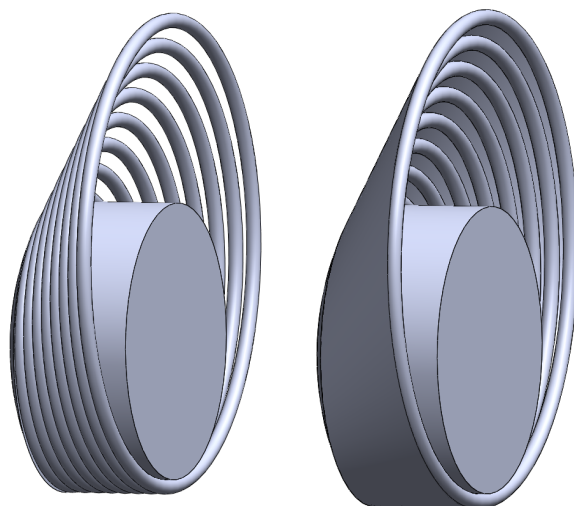


Figure 10. Demonstration of FlexShell gap closure.

In order to create a stronger FlexShell, one large sheet of Kevlar will be used with a single seam connecting the edges to create the three dimensional shape. This seam will run along the vertical part of the HIAD, next to the tori that are tangent to each other and the cylindrical payload fairing.

Packing the tori and FlexShell will require a different packing configuration than the symmetric HIAD. In this new configuration, the inflatable structure will be packed around the cylindrical payload fairing rather than around the nose of the vehicle. This will require a secondary cloth cover that keeps the tori and FlexShell compacted, also protecting it from micrometeor and orbital debris damage. This cloth cover will be jettisoned prior to HIAD inflation.

C. Structural Analysis

Structural analysis was used to validate the integrity of the chosen design shape, which is defined using two metrics: maximum deflection and maximum stress. The Patran/Nastran software package from MSC was used for the analysis. The first step was to import the geometric information required to construct the model from the mass calculations. Once the geometry was created, the material properties were assigned to their corresponding components. Since it was assumed that both the FlexShell and the tori were made of Kevlar, only one material property was required for this model, with isotropic material properties shown in Table 6.²⁵ Following the material definition, the next step was to mesh the geometry. The mesh size can be chosen based on the size of the overall structure as well as individual components. Since the first torus was assumed to be fixed to the rigid nose cone, fixed boundary conditions were applied to all the nodes on the first torus that were in contact with the nose cone. An additional fixed boundary condition was also applied to simulate the fact that all of the tori along the short side (L) were attached to the payload cylinder. There were two loading conditions applied to the model: internal inflation pressure and external dynamic pressure. An internal inflation pressure of 15 (psi) was applied to the interior of all tori and the external dynamic pressure was applied to the outside of the flexible wrap. The magnitude of external dynamic pressure corresponded to the maximum dynamic pressure obtained from the trajectory simulation 17.5 kPa, as detailed in Section E. The finite element model was solved in Nastran and the results were imported back to Patran for post-processing.

Table 6: Kevlar Material Property

Elastic Modulus (Pa)	Poisson Ratio	Shear Modulus (Pa)	Density (kg/m^3)
3E9	0.36	1.1E9	1150

As shown in Figure 11, the maximum displacement occurred on the largest torus with a maximum value of 1.22 mm. This displacement corresponded to 0.008% of the 15 (m) HIAD major diameter. The stress resulted from the imposed fixed boundary conditions along the shortest side (L) of the HIAD. The Von Mises stress results are also included, seen in Figure 11.

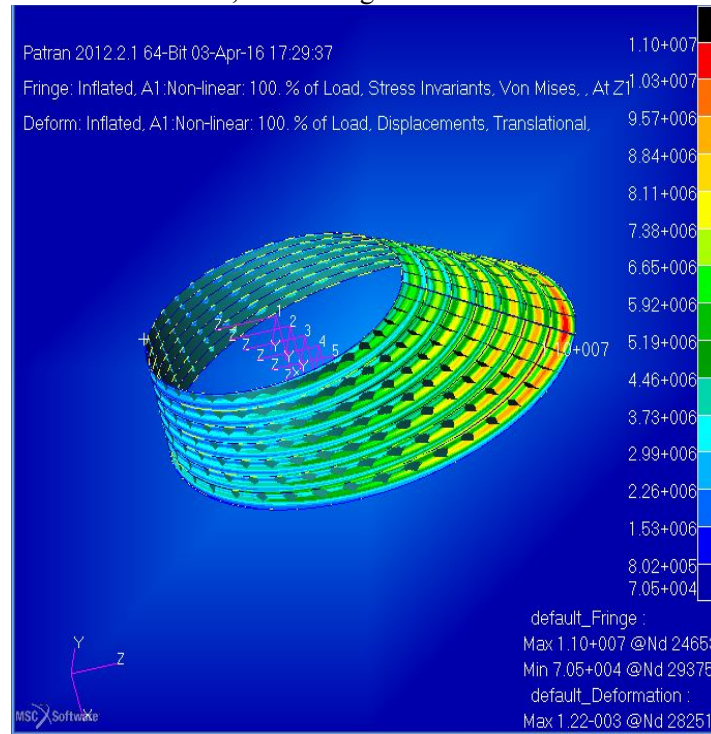


Figure 11: Max deflection and Von Mises Results

This model demonstrates the first steps towards developing a full finite element analysis of the inflatable aeroshell. Both the overall deflection and resulting stresses will be analyzed to better understand the structural performance of the proposed design.

Preliminary structural results were estimated for this study using modified versions of the structural equations found in the IAD dimensionless mass estimation study.³⁰ In the derivation of the IAD mass, four different structural capabilities were defined and derived: inflatable structure resistance to external loading, inflatable torus fabric strength, gore fabric strength, and radial strap strength. The equations for these parameters were derived assuming an axisymmetric inflatable aeroshell. As a result, it was required to re-derive these equations in order for them to be applicable to the asymmetric shifted HIAD configuration proposed by this project.

The calculations for the inflatable structure resistance to external loading estimate the minimum inflation pressure required to ensure zero circumferential stress in the membrane under maximum loading.³¹ The calculations use the principal of virtual work to equate the work done by an external aerodynamic load (F_A) through a structural displacement (δ) and the volume change (dV) of inflation gas multiplied by the inflation pressure (P) as a result of a cone angle deflection. The principal of virtual work is formulated via Equation 11. The following calculations for the asymmetric vehicle differed from the original calculations. The structural displacement (δ) can be determined from θ and D_0 as in Equation 12.

$$F_A \partial \delta = -P \partial V \quad (11)$$

$$\delta = \frac{2D_0}{3 \tan(\theta)} \quad (12)$$

The gas volume of the decelerator can also be estimated by relating the asymmetric design to its equivalent symmetric design. The shifted HIAD geometry is achieved by displacing successive tori so that they are tangent along L . These tori can also be re-arranged to form a symmetric shape, which

because it is composed of the same inflatable members, will have the same inflated volume. The relationship between the asymmetric (θ) and symmetric (θ_s) cone angles is described in Equation 13 and the inflated volume is calculated in Equation 14.

$$\theta_s = \tan^{-1} \left(\frac{\tan(\theta)}{2} \right) \quad (13)$$

$$V = \frac{\pi D_0^2 r}{4 \sin(\theta_s)} \quad (14)$$

These parameters can then be used in the virtual work relation (Equation 11) to solve for the required inflation pressure, as seen in Equation 15. In this equation the dynamic load is taken to be the drag load $qC_D A_{ref}$ from the dynamic pressure (q), drag coefficient (C_D), and reference area (A_{ref}).

$$P_{min} = \frac{2qC_D A_{ref} \sin^2(\theta_2)(3\cos(2\theta)+5)}{3\pi D_0 r \cos(\theta_2)} \quad (15)$$

For the design parameters from the aerodynamic and mass analyses, the required P_{min} was 24 (psi). The inflatable torus fabric strength calculations were not re-derived in this study because testing of inflatable tori has been conducted to pressures exceeding the required minimum pressure. The gore fabric strength calculations were also not considered. In the original derivation, the gore was intended to support the local surface pressure while radial straps were used to support the decelerative loading. In the current proposed design, the FlexShell is intended to satisfy both requirements. Of the two conditions, it is expected that the decelerative loading will be the dominant constraint. Therefore, the FlexShell structural performance is assessed via the radial strap relations from the original paper.

The following calculations for the asymmetric vehicle differed from the original calculations. The maximum stress on flex cover will occur along the attachment to the rigid nose cone because it has the smallest cross-sectional area and experiences the full load. The stress (σ) in this region is described by Equation 16, where θ_H is the local FlexShell angle and dl is the infinitesimal circumference. The local FlexShell angle can be described by Equation 17, where ϕ is an angle centered in the middle of the largest torus with $\phi = 0$ pointing towards the shortest edge.

$$\sigma = \frac{F_{Drag}}{\int \cos(\theta_H) t \, dl} \quad (16)$$

$$\tan(\theta_H) = \frac{\sqrt{1-\cos(\phi)} \tan(\theta)}{\sqrt{2}} \quad (17)$$

The circumference is therefore $dl = \frac{D_N}{2} d\phi$ and the stress can be described via Equation 18, with $F(x|m)$ being the elliptic integral of the first kind with parameter $m = k^2$.

$$\sigma = \frac{qC_D A_{ref}}{D_N t F(-\tan^2(\theta))} \quad (18)$$

The specified design parameters resulted in a stress of 0.047 GPa. Therefore, the tensile stress in the FlexShell was less than the FlexShell tensile strength (Kevlar, $\sigma_Y = 3$ GPa from Table 6), which demonstrated that the FlexShell has the potential to support full aerodynamic loading during entry. Alternatively, this relation can also be used to determine the maximum sustainable dynamic pressure loading. Assuming that the FlexShell has a yield strength of 3 GPa, the maximum possible loading for the proposed geometry is 8.37 MPa, which is calculated from Equation 18. Overall, the structural analysis showed that the shifted HIAD design proposed in this study has sufficient structural strength. In the future, the structural capability of the proposed design will be assessed with additional high fidelity finite element analysis.

D. Lift to Drag Modulation

The benefits of an additional technology package that could be added to the HIAD and would enable in flight L/D modulation was investigated. The benefits of such an addition to a high L/D reentry vehicle are numerous. By modulating the L/D ratio, the entry trajectory becomes more controllable. It was also found that high lifting trajectories cause the vehicle to skip out of the atmosphere, modulating the L/D ratio to a lower value in flight might prevent this skipping.

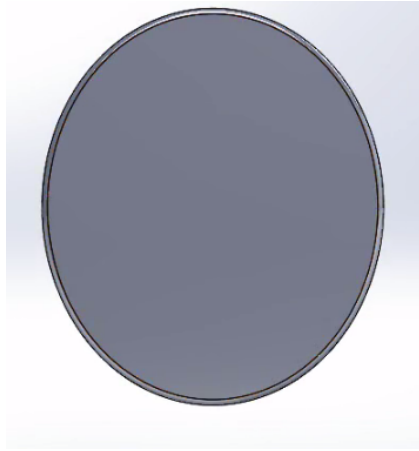


Figure 12: Shape morphing design.



Figure 13: Trim tab design



Figure 14: Extendable bladder design.

Three modulation techniques were investigated and their performance and risks were compared. The first design was a shape morphing design, shown in Figure 12, in which the circular cross section of the inflatable became an ellipse. The second design was a trim tab, shown in Figure 13, which attached to the back of the vehicle on the payload cylinder. The third was a bladder placed beneath the rigid heat shield, shown in Figure 14, which could be inflated to change the shape of the rigid heat shield. These shapes were modeled and aerodynamic analyses were performed. The results of the analysis were compared to the baseline design of an asymmetric design with cone angle of 65° , major diameter of 15 m, and rigid nose diameter of 9 m. It was found that the extendable bladder design produced negligible change to the L/D ratio at the baseline configuration. Both the trim tab and the shape morphing designed showed similar and promising results in the aerodynamic analysis, therefore the design simplicity associated with using each method and complexity in the construction were considered.

The shape morphing design requires the vehicle to be deformed, which may result in the folding and bunching of fabric and eventually localized heating. Creating a mechanism for the morphing would additionally add a layer of complexity to the construction of the vehicle. The trim tab method would similarly have consideration in the construction, but could be added to the back of the payload cylinder. This would avoid any localized heating issue. Because the shape morphing design was believed to have more risk associated with the design, the trim tab was investigated further.

The size of the trim tab was varied to investigate the effect on L/D, and the results are shown in Table 7. As the diameter of the trim tab increases, the L/D ratio and the trim angle of attack decrease. It was also found that when the baseline L/D was lower the trim tabs had a greater effect on L/D ratio modulation.

Table 7: Resulting L/D Modulation for Baseline Configuration (L/D = 0.5)

Trim Tab Diameter (m)	L/D	$\alpha_{\text{trim}} (^\circ)$	CG off center line [%]
No Tab	0.500	-29	36
0.5	0.471	-26	36
1.0	0.441	-23	36

The selected optimized geometry successfully achieves the maximum L/D requirement and the pitch static stability requirement.

E. Trajectory Flight Envelope

After the method of lift modulation had been determined, a trajectory analysis was conducted using the Aeroassist Simulation (ASIM), developed in the Georgia Tech Space Systems Design Laboratory (SSDL) over many years. The analysis utilizes first order approximation equations of entry to generate predicted entry trajectories. In this study, ASIM was configured to generate lifting trajectories in the Martian atmosphere using a Mars Global Reference Atmospheric Model (MARSGRAM) atmospheric model. Aerodynamic information obtained for the final shape of an asymmetric vehicle with a cone angle of 65° , major diameter of 15 m, and rigid nose diameter of 9 m was also incorporated into the trajectory simulation.

As a first approximation, the Mars Science Laboratory (MSL) entry conditions were used, which corresponds to an entry velocity of 6 (km/s) and an entry flight path angle of -15.2° relative to the local horizontal at a Mars entry interface altitude of 125 (km). The analysis in Section II discusses in detail how the HIAD concept can generate a lift-to-drag ratio of 0.5. Additionally, a bank angle of 65° was chosen to prevent atmospheric skip-out due to the large vertical component of the lift vector. The resulting trajectory, with a bank angle of 65° , is shown in Figure 15 and Figure 16 by displaying altitude as a function of relative velocity and downrange, respectively.

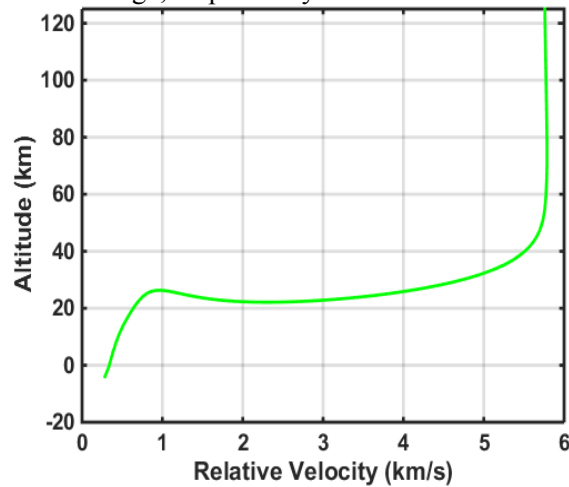


Figure 15: Altitude vs. Relative Velocity for Nominal Trajectory at $L/D = 0.5$

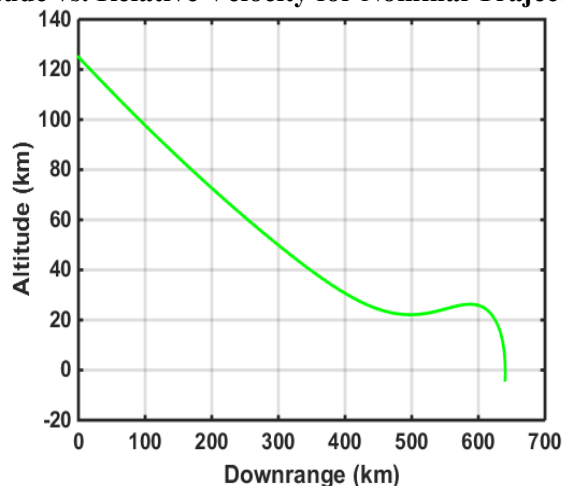


Figure 16: Altitude vs. Downrange for Nominal Trajectory at $L/D = 0.5$

For this trajectory, the resulting maximum dynamic pressure and maximum heat flux are approximately 17.5 (kPa) and 55 (W/cm^2), respectively. The structural analysis of the selected HIAD

vehicle shows that it can withstand a maximum loading of 706 kPa and past thermal analysis shows that previous Flexible Thermal Protection System (FTPS) for HIADs can withstand a heat flux up to 60 (W/cm^2).²⁴ Therefore, this nominal trajectory is feasible from both structural and thermal standpoints.

The following analysis shows the flight envelope between the maximum and minimum lift-to-drag ratio configurations. The entry conditions are assumed to be identical to MSL entry conditions for all trajectories. The resulting trajectories for lift-to-drag ratio configurations of 0.5 and 0.2 are shown in Figure 17 through Figure 19.

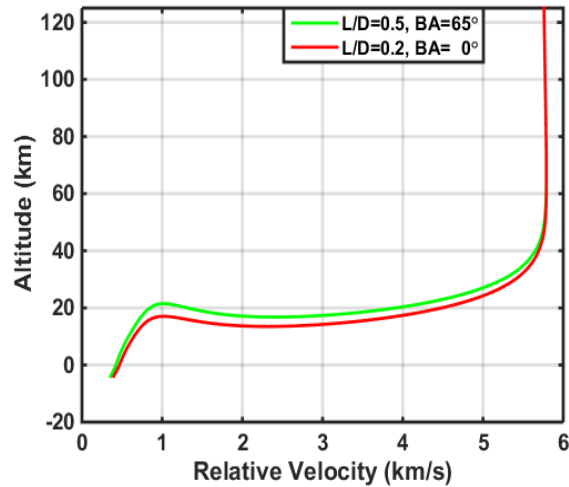


Figure 17: Altitude vs. Rel. Vel. for Nominal Trajectories at $L/D = 0.5$ and $L/D = 0.2$

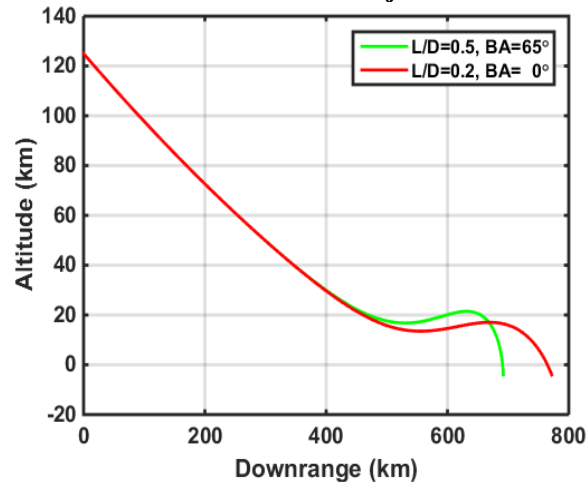


Figure 18: Altitude vs. Downrange for Nominal Trajectory at $L/D = 0.5$ and $L/D = 0.2$

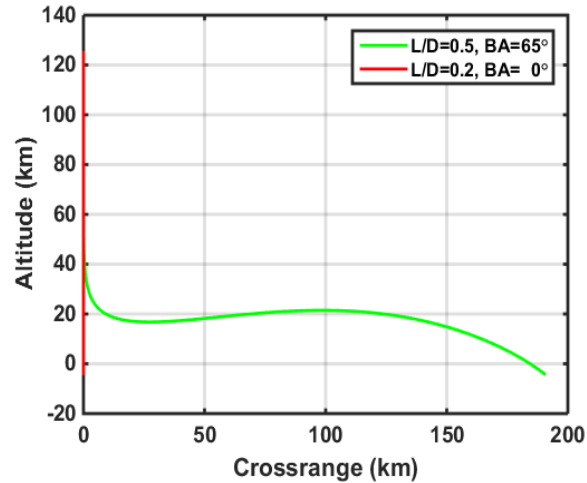


Figure 19: Altitude vs. Crossrange for Nominal Trajectories at $L/D = 0.5$ and $L/D = 0.2$

It is important to note that the lift-to-drag ratio of 0.2 is achieved by holding a bank angle of 0° . In this situation, the vertical component of the lift vector is small and the vehicle is not at risk for atmospheric skip-out. Therefore, a bank-angle is not required to remain on a direct entry trajectory through the atmosphere. However, when the lift-to-drag ratio is 0.5, a bank angle of 65° is required to prevent atmospheric skip-out, which produces a crossrange component. This crossrange component can be accounted for before entry or it can be mitigated during flight if the vehicle holds a bank angle of -65° for a significant amount of time. Overall, this trajectory analysis confirms that the desired range of entry trajectories are feasible and favorable for landing high-mass payloads on the surface of Mars.

F. Extensibility to Large Scale Operation

A full-scale vehicle was considered in order to provide a comprehensive evaluation of a given design's feasibility. The payload has been assumed to be approximately 20 metric tons and asymmetric HIAD concepts with diameters between 15 m and 20 m have been considered. The final selected concept has a major diameter of 15 m. The results from this study have indicated that the final selected concept is feasible and meets the specified design constraints. In the future, the presented analysis will be repeated for diameters larger than 20 m to confirm the scalability of the presented HIAD design.

IV. Next Steps for Analysis on Proposed HIAD Concept

A. Next Steps for Current Asymmetric HIAD Design

The analysis conducted in this study can be extended to improve the performance and feasibility of the proposed concept. For example, the HIAD geometry selection process can consider shapes that target positioning the vehicle's CG along the centerline of the cylindrical payload fairing. The main benefit would be reduced packing constraints on the payload and full utilization of payload fairing internal volume. Figure 20 shows how the pitching moment coefficient changes with angle-of-attack if the CG is fixed along the centerline of the cylindrical payload fairing (at $(x, y, z) = (2.34, 0, 0)$). By using trends seen in Figure 20, an L/D of over 0.5 can be achieved with static stability about the pitch axis at an angle-of-attack of -62.5° , which is shown in Figure 21 and Figure 22.

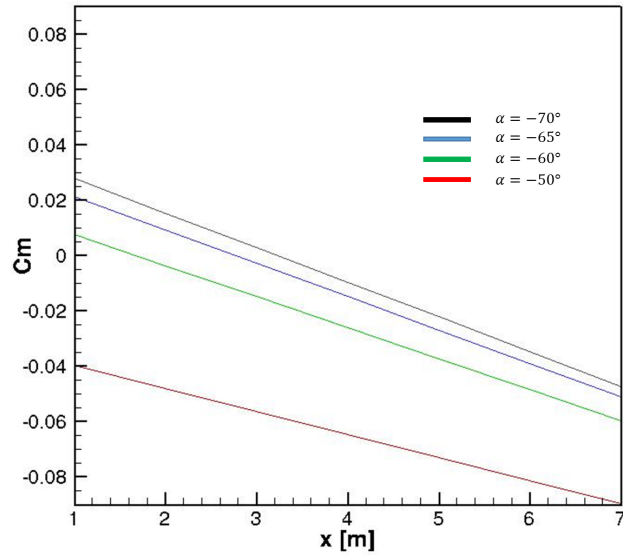


Figure 21: Pitching Moment Coefficient (C_m) with Potential CG Locations

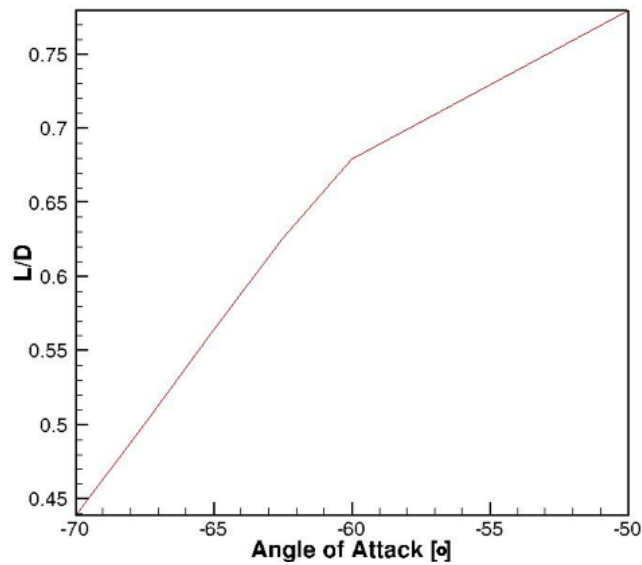


Figure 22: L/D vs. Angle-of-Attack

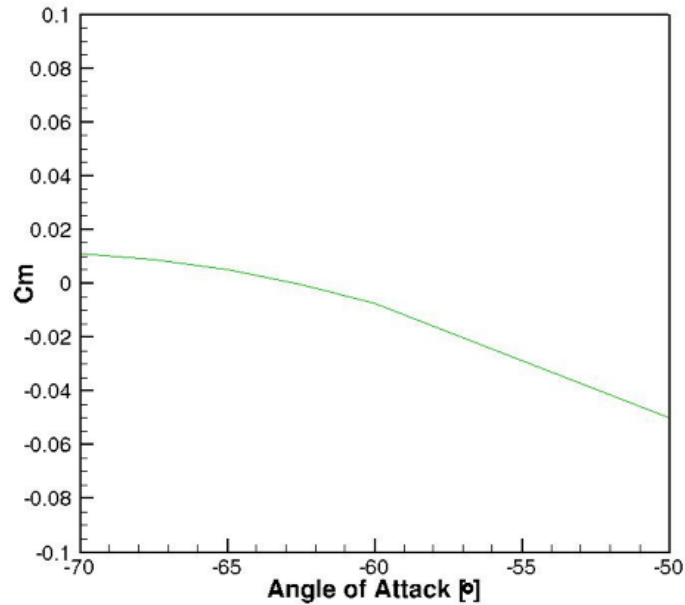


Figure 23: Pitching Moment Coefficient (C_m) at CG Location (2.34, 0, 0)

The development of the fabrication and assembly processes of the FlexShell will be an ongoing process. The FlexShell is comprised of a continuous, single-sheet of high-density Kevlar. As a result, it is likely to contribute significantly to the inflatable structure mass, which can be considered in a more comprehensive objective function, as defined in Equation 3. Additionally, more development is necessary to find the most effective method of stitching the FlexShell to the tori. Examining the stitching pattern, stitching material, and attachment point locations are all considerations for the next round of analysis.

Further trajectory analysis is necessary to ensure that peak heating and dynamic pressures do not exceed vehicle limitations. A single event drag modulation will also be compared to the lift modulation trajectory to determine if similar trajectories can be produced with both methods.

The ultimate goal of this analysis will be to create a robust HIAD system certified for implementation on future missions, and to expand HIAD technology to the point where it can be implemented in Mars surface missions. Future steps of this design will consist of 3 phases: concept studies and vehicle design, extensive ground testing, and a flight test to certify the system. The concept studies will evaluate potential HIAD designs outlined in this work, with the goal of selecting a single optimal design for further development. Computer simulations, spacecraft modeling, and cost and simplicity evaluations will be used to decide upon the ideal configuration for the flight vehicle.

V. Conclusion

This technical paper presented a system-level study of a new HIAD concept geometry designed to minimize the required trim angle of attack to achieve an L/D of 0.5. A novel “100% shifted HIAD” stacked tori configuration was identified, analyzed, and shown to be an attractive and feasible design. This geometry achieves static aerodynamic stability about the pitch axis in desired flight regime. Through the use of a pre-launch vehicle design methodology, technology package additions, and bank angle modulation, the proposed HIAD design has the capability to modulate L/D from 0.2 to 0.5.

After performing a study to balance HIAD mass and complexity for the final HIAD configuration, it was found that eight tori most effectively minimized the overall objective function. A sensitivity analysis was also performed to determine the effects of weighting different combinations of final design parameters. Results show that system complexity weighting has little effect on the objective function due to external constraints, while the system mass weighting has a large effect on selection of final design parameters. The presented structural analysis used two approaches to evaluate the structural performance

of the chosen configuration. Finite element analysis showed that the tori can withstand inflation loading up to 15 (psi). A novel aeroshell system, called the FlexShell, covers the external surfaces of all tori to maintain the desired geometry and distribute structural loads evenly. Analytic approximations showed the HIAD to have sufficient resistance to deflection and demonstrate that the FlexShell can withstand the maximum aerodynamic loading obtained from trajectory simulations. A detailed trajectory analysis determined that the expected values of peak dynamic pressure and peak heating can be withstood by the vehicle's structural components and Flexible Thermal Protection System (FTPS), respectively.

Acknowledgments

The authors thank Dr. Stephen Ruffin and Alex Longo for their generous contributions to this research effort. Additionally, the authors thank Tyler Anderson, Casey Heidrich, Adam Sidor, and all other members of the SSDL that contributed to the analysis presented in this paper. Finally, the authors are grateful for all those participating in the HIAD research and development effort. Thank you for making this research possible.

References

- [1] Braun, R. D., and Manning, R. M., "Mars Exploration Entry, Descent, and Landing Challenges," *Journal of Spacecraft and Rockets*, Vol. 44, No. 2, March–April 2007, pp. 310–323. doi:10.2514/1.25116
- [2] D. W. Way, R. W. Powell, A. Chen, A. D. Stelzner, A. M. San Martin, P. D. Burkhart, and G. F. Mendeck, "Mars Science Laboratory: Entry, Descent, and Landing System Performance," *IEEE Aerospace Conference*, 2006.
- [3] Adler, M. et al, "Draft Entry, Descent, and Landing Roadmap: Technology Area 09," NASA, November 2010.
- [4] Dwyer-Cianciolo, Alicia M., et al. "Entry, Descent and Landing Systems Analysis Study: Phase 1 Report." (2010).
- [5] Ivanon, M. C., et al, "Entry, Descent, and Landing Systems Analysis Study: Phase 2 Report on Mars Science Laboratory Improvement," NASA/TM-2011-216988, July 2011.
- [6] Steinfeldt, B. A., et al, "High Mass Mars Entry, Descent, and Landing Architecture Assessment," AIAA 2009-6684, AIAA Space 2009 Conference and Exposition, Pasadena, CA, September 2009.
- [7] Drake, B. G. (Editor), "Human Exploration of Mars Design Reference Architecture 5.0," NASA/SP-2009-566, July 2009.
- [8] Andrews, D. G., Cannon, J. H., Lund, E. A., Watry, K. E., "High Mass Mars Entry System: Architecture Design and Technology Development Roadmap," NASA/CR-2009-NNL08AA35C, September 2009.
- [9] Smith, B. P., Tanner, C. L., Mahzari, M., Clark, I. G. Braun, R. D., and Cheatwood, F. M., "A Historical Review of Inflatable Aerodynamic Decelerator Technology Development," *IEEEAC 1267*, 2010 IEEE Aerospace Conference, Big Sky, MT, March 2010.
- [10] Stephen J. Hughes, Robert A. Dillman, Brett R. Starr, Ryan A. Stephan, Michael C. Lindell, Charles J. Player, and F. McNeil Cheatwood: "Inflatable Re-entry Vehicle Experiment (IRVE) Design Overview", 18th AIAA Aerodynamic Decelerator Systems Technology Conference and Seminar, Munich, Germany, May 24-26, 2005.
- [11] Michael C. Lindell, Stephen J. Hughes, Megan Dixon, and Cliff E. Willey, "Structural Analysis and Testing of the Inflatable Re-entry Vehicle Experiment (IRVE)", AIAA-2006-1699
- [12] Starr, B. R., Bose, D. M., Thornblom, M., and Kilcoyne, D. "Inflatable Reentry Vehicle Experiment Flight Performance Simulations," 53rd JANNAP Propulsion Meeting, Monterey, CA, Dec. 5-8, 2005.
- [13] Stephen J. Hughes, Joanne S. Ware, Joseph A. Del Corso, and Rafael A. Lugo "Deployable Aeroshell Flexible Thermal Protection System Testing", 20th AIAA Aerodynamic Decelerator Systems Conference, May 2009.

- [14] Stephen A. O’Keefe and David M. Bose, “IRVE-II Post-Flight Trajectory Reconstruction”, AIAA-2010-7515 AIAA Atmospheric Flight Mechanics Conference, Toronto, Ontario, Aug. 2-5, 2010.
- [15] Robert A. Dillman, Stephen J. Hughes, Richard J. Bodkin, David M. Bose, Joseph Del Corso, and F. McNeil Cheatwood: “Flight Performance of the Inflatable Reentry Vehicle Experiment II”, 7th International Planetary Probe Workshop, Barcelona, Spain, June 14–18, 2010.
- [16] O’Keefe, S. A., Bose, D. M., “IRVE-II Post-Flight Trajectory Reconstruction,” AIAA Atmospheric Flight Mechanics Conference, AIAA Paper 2010-7515, 200914 O’Keefe, S. A., Bose, D. M., “IRVE-II Post-Flight Trajectory Reconstruction,” AIAA Atmospheric Flight Mechanics Conference, AIAA Paper 2010-7515, 2009.
- [17] Harper, Braun, “Asymmetrically Stacked Tori Hypersonic Inflatable Aerodynamic Decelerator Design Study for Mars Entry”, AIAA Atmospheric Flight Mechanics Conference. National Harbor, MD 2014.
- [18] Brooke P. Harper, Dr. Robert D. Braun, “Preliminary Design Study of Asymmetric Hypersonic Inflatable Aerodynamic Decelerators for Mars Entry”
- [19] Mars Atmosphere Model - Metric Units – NASA Website URL: <https://www.grc.nasa.gov/www/k-12/airplane/atmosmrm.html>
- [20] Anderson, J. D. J., “Hypersonic and High Temperature Gas Dynamics”, McGraw-Hill, New York, 1989.
- [21] Mars Atmosphere Model - Metric Units – NASA Website URL: <https://www.grc.nasa.gov/www/k-12/airplane/atmosmrm.html>
- [22] Mars Fact Sheet –NASA Website URL: <http://nssdc.gsfc.nasa.gov/planetary/factsheet/marsfact.html>NASA mars air
- [23] Myers, R. H., Montgomery, D. C., Anderson-Cook, C. M., “Response Surface Methodology: Process and Product Optimization Using Designed Experiments,” 3rd Edition, Wiley.
- [24] Hughes, S. J., Cheatwood, F. M., Dillman, R. A., Wright, H. S., DelCorso, J. A., and Calomino, A. M., “Hypersonic Inflatable Aerodynamic Decelerator (HIAD) Technology Development Overview,” 21st AIAA Aerodynamic Decelerator Systems Technology Conference and Seminar, Dublin, Paper 2011-2524, May 2011.
- [25] “Technical Guide – Kevlar – Aramid Fiber”, DuPont, 2016. URL: http://www.dupont.com/content/dam/dupont/products-and-services/fabrics-fibers-and-nonwovens/fibers/documents/Kevlar_Technical_Guide.pdf
- [26] Cassell, A. M, Swanson, G. T., Johnson, R. K., Hughes, S. J., and Cheatwood, F. M., “Overview of the Hypersonic Inflatable Aerodynamic Decelerator Large Article Ground Test Campaign,” AIAA 2011-2569, 21st AIAA Aerodynamic Decelerator Systems Technology Conference, and Seminar, May 2011.
- [27] “Three-Dimensional Shapes: Polyhedrons, Curved Solids and Surface Area”, SkillsYouNeed.com. URL: <http://www.skillsyouneed.com/num/3d-shapes.html>
- [28] Ashley M. Korzun, Gregory F. Dubos, Curtis K. Iwata, “A Concept For The Entry, Descent, And Landing of High-Mass Payloads at Mars”, URL: <http://www.ssd.l.gatech.edu/papers/conferencePapers/IAC-2008-D2.3.9.pdf>
- [29] Lyle, K.H., “Comparison of Analysis with Test for Static Loading of Two Hypersonic Inflatable Aerodynamic Decelerator Concepts”, NASA/TM-2015-218778, Jul. 01, 2015.
- [30] Samareh, J., A., “Estimating Mass of Inflatable Aerodynamic Decelerators Using Dimensionless Parameters.” 8th International Planetary Probe Workshop (IPPW-8). Portsmouth, VA. 6-10 June, 2011.
- [31] Brown, G. J., “Estimating Minimum Inflation Pressure for Inflatable Aerodynamic Decelerators,” AIAA-2009-2970 (revised on June 8, 2009).
- [32] Vanessa Dorado, Zachary Grunder, Bryce Schaefer, Meagan Sung, Kevin Pedersen, “NASA Marshall Space Flight Center Tri-gas Thruster Performance Characterization”
- [33] Olds, A. D., “IRVE-3 Post Flight Test Reconstruction,” AIAA Paper 1514242, Mar 25, 2013.
- [34] Overview of the 6 Meter HIAD Inflatable Structure and Flexible TPS Static Load Test Series, IPPW
- [35] Johansen, C. T., Novak, L., Bathel, B., Ashcraft, S.W., and Danehy, P. M., “Comparison of MSL RCS jet computations with flow visualization and velocimetry,” AIAA Paper 2012-0594, Jan. 9th 2012.